

RSC Advances



This is an *Accepted Manuscript*, which has been through the Royal Society of Chemistry peer review process and has been accepted for publication.

Accepted Manuscripts are published online shortly after acceptance, before technical editing, formatting and proof reading. Using this free service, authors can make their results available to the community, in citable form, before we publish the edited article. This *Accepted Manuscript* will be replaced by the edited, formatted and paginated article as soon as this is available.

You can find more information about *Accepted Manuscripts* in the [Information for Authors](#).

Please note that technical editing may introduce minor changes to the text and/or graphics, which may alter content. The journal's standard [Terms & Conditions](#) and the [Ethical guidelines](#) still apply. In no event shall the Royal Society of Chemistry be held responsible for any errors or omissions in this *Accepted Manuscript* or any consequences arising from the use of any information it contains.

Controlled Removal of Monolayers for Bilayer Graphene

Preparation and Visualization

Lin Gan^{1,a}, Haijing Zhang^{2,a}, Ruizhe Wu¹, Yao Ding¹, Ping Sheng² and Zhengtang

Luo^{1,*}

¹Department of Chemical and Biomolecular Engineering, The Hong Kong University of Science and Technology, Clear Water Bay, Kowloon, Hong Kong

²Department of Physics and William Mong Institute of Nano Science and Technology, The Hong Kong University of Science and Technology, Clear Water Bay, Kowloon, Hong Kong, China

Email: keztluo@ust.hk

a) These authors contributed equally to this work.

Abstract Bilayer graphene, unlike monolayer graphene, provides a tunable electronic energy gap when an electrical field is applied across the layers, therefore holds great potential in semiconductor industry. Here, we demonstrate a facile technique to obtain bilayer graphene structures on the growth substrate by controlling oxidation to remove monolayers, while retaining the bilayer electronic properties. We found that this precise oxidation process selectively destructs monolayers while preserves the qualities of bilayers, evidenced by the expected quantum hall effect and exceptional room temperature carrier mobilities of $\sim 3500 \text{ cm}^2 \text{ v}^{-1} \text{ s}^{-1}$ obtained from electrical transport measurement. In addition, visualization of bilayers, which serves as nuclei for graphene growth, opens the door for the understanding the actual mechanism of graphene growth process which eventually can lead to the optimized synthesis.

1 **Introduction**

2 Graphene is a promising material for electronic applications, but their intrinsic gapless
3 semimetal nature hurdles their applications in semiconducting industry. On the other
4 hand, bilayer graphene, in particular for AB Bernal stacking order, can provide a
5 tunable bandgap when an electrical field is applied across the layers, hence forth
6 attracted considerable attention for its potential application in logic circuit¹⁻³. To
7 obtain large size graphene thin films for practical applications, Chemical Vapor
8 Deposition (CVD) method⁴⁻⁶ was developed to synthesize monolayer graphene thin
9 films, which was later extended for bilayers or few layers graphene preparation.
10 However, current processes always produce graphene films that contain a significant
11 portion of monolayer, which will have detrimental effects when used in
12 semiconductor devices. Moreover, it would be also desirable to directly observe the
13 structure and overall distribution of graphene nuclei during CVD growth, in order to
14 understanding the underlying kinetics for graphene growth. Previously, a simple
15 optical method has been developed to directly visualize monolayer graphene grains on
16 Cu foil, taking advantage of their different contrast between graphene-covered and
17 uncovered region after mild oxidation⁷. However, visualizing bilayer graphene has not
18 been reported so far, due to the difficulties of gaining contrast between bilayer and
19 monolayer graphene. Consequently, characterization methods for bilayers on Cu
20 substrate are mainly limited to localized methods such as scanning electron
21 microscopy (SEM)⁸ and atomic force microscopy (AFM)⁹, which precludes us from
22 obtaining a full map of graphene distribution on copper substrate, or limiting us to an

1 optical method by transferring the post-synthesized graphene onto silicon wafer of
2 300 nm SiO₂¹⁰.

3 Here we show a simple method that enables us to solve the purification and direct
4 visualization issue at the same time. This is achieved by controlling the oxidization of
5 the post-growth monolayer and bilayer graphene/Cu substrate in air at a raised
6 temperature, utilizing their different resistance to oxidation. Controlled oxidation
7 renders the Cu metal covered by monolayer easily oxidized, while area covered by the
8 bilayers are only insignificantly affected, and consequently leads to the contrast for
9 the monolayer and bilayer covered region. Electron transport measurement on
10 bilayer-based FET devices confirms that the quality of bilayers are well preserved
11 during this controlled oxidation process.

13 **Results and Discussions**

14 We firstly demonstrate a controlled oxidation method by showing the evolution of
15 graphene grains during this process. **Figure 1** illustrates a sequence of optical images
16 recorded at end of annealing at 200°C for 30s, followed by annealing in air at 300°C
17 for additional 30s, 60s, 90s and 120s, respectively. At the early stage of annealing, the
18 contrast of monolayer to copper substrate gradually increases and reached a maximum
19 after annealing at 300°C for ~60s concurrent with the observation that copper
20 substrate turning from red to light green in this process (for more images, see fig. S1
21 of Supplementary Information). Additional annealing at 300°C for 90s induces a
22 sudden decrease in contrast between monolayers and copper substrate, while

1 simultaneously reveals the bilayer nucleus in the center of the graphene grain. After
2 additional annealing at 300°C for 120s, majority of the monolayers are broken into
3 fragments and the nucleus stand out sharply. In addition, we note that a significant
4 number of cracks emerge along the edges of nucleus, as shown in figure 1f, implying
5 that the oxidation for nucleus may start from the edges. Similar result can be obtained
6 if lower annealing temperature but longer duration is used, for example, after
7 exposing the graphene/Cu sample in air for several months (fig. S2 of Supplementary
8 information), the nuclei also become visible.

9 **Figure 2** illustrates the detailed surface morphology acquired by atomic force
10 microscope (AFM). The after-oxidation morphology of regions that were previously
11 covered by monolayer, *i.e.* in the outer part of the graphene (fig. 2b and corresponding
12 profile in 2d) shows that monolayer grain has been broken into fragments, possibly
13 are damaged by the copper oxide particles or stripes formed after the oxidation,
14 whereas the bilayer nucleus are intact with only a few insignificant damages (fig. 2c
15 and corresponding profile in 2d), consistent with the result shown in figs 1f. The
16 formation of oxide particles or stripes after oxidation has been elaborately studied by
17 many groups^{5, 11-12}(also see XPS results in Figure S6 of supplementary information)
18 and the size ranges from nanometer to micrometer scales, depending on degree of
19 oxidation and temperature. As a result of nanoparticle's volume expansion, stress will
20 be induced on the monolayer graphene, which also leads to their reactivity
21 enhancement. Following the oxidation on those sites, defects and cracks will expand
22 to larger cracks, which allows more exposure to oxygen for the Cu substrates. As

1 shown in figure 2a, a crack are also occasionally seen on some bilayers regions, but
2 typically has limited effect on electronic quality as will be shown in latter part of the
3 discussion.

4 The method reported here provides insights on possible oxygen diffusion path
5 during the oxidation. Previously study has shown that graphene is impermeable for
6 most gas, including helium¹³. Therefore, the most likely paths for oxygen to attack the
7 graphene-covered region are 1) from above through defects or atom exchange
8 mechanism¹⁴, or 2) from bottom through the micro-space/ripples formed between
9 grains and copper substrate. One would expect the former path is more common, as
10 defective sites usually has high reactivity, as it was observed that the methane
11 decomposition usually started at those defective sites which includes impurities¹⁵,
12 metal step¹⁶ or metal particles⁵. This diffusion path, however, does not agree with our
13 experimental observation that only insignificant damage were observed at the nucleus
14 center, while the majority of cracks are near the edges. Instead, our observation
15 supports that oxygen may attack the monolayers from underneath. Indeed, micrometer
16 scale periodical ripples^{5, 8} are widely seen for CVD-grown graphene due to the
17 thermal expansion coefficient mismatch between graphene and copper substrate
18 during cooling process. Those ripples form easy accessible channel for oxygen
19 diffusion (Fig. S3 of Supplementary Information). Nevertheless, the oxygen path may
20 also dependent on the temperature, as crack and pits are also seen in the graphene
21 terrace when the sample is placed in air at room temperature for an extended period
22 (Fig. S2 of Supplementary information). In addition, electrochemical erosion may

1 have also involved in this process¹⁷.

2 **Figure 3** depicts further characterization of the visualized bilayer/few layers
3 graphene structure. Figure 3a illustrates the scanning electron microscopy (SEM)
4 image of a typical bilayer/few layers graphene flake synthesized by CVD⁵, which
5 were embedded at the center of a large single crystal graphene monolayer (inset of Fig.
6 3a). The monolayer graphene shows asymmetric structure of diameter ~1mm,
7 consistent with our previous report. After annealing the sample in air under 300 °C
8 for 2 minutes, intense contrast were obtained for the bilayer nucleus at the center,
9 where the monolayer-covered region become less reflective and turned to dark color,
10 as shown in Fig. 3b (see more images at Fig. S4 in the supplementary information
11 section). As will be clarified later from Raman measurement, this originated from the
12 destruction of the monolayer, concurrent with copper substrate oxidation. By using
13 this method, the nucleus region stands out sharply against original graphene flake
14 region, due to the contrast resulted from reduced reflectance. Interestingly from this
15 visualization method, we observed some individual hexagonal shape grains have more
16 than one nucleus in the center (Supplementary Fig.S2), contrary to common belief
17 that each graphene flake was grown from a single nucleus. More work is in progress
18 to understand this phenomenon.

19 To understand the nature of graphene nucleus, we performed the Raman
20 characterization on the sample after it was transferred onto 300 nm oxides thickness
21 silicon wafer. As shown in **Figure 3c**, the outer region of the original graphene flakes
22 show mostly broken graphene fragments. Single point Raman spectrum at site 1,

1 shown in figure 3d, displays an enhanced D peak ($\sim 1350\text{ cm}^{-1}$) for monolayer
2 graphene, with typical monolayer G and 2D bands appears at 1580 and 2680 cm^{-1} ,
3 respectively. In contrast, Raman spectrum at sites 2 and 3 reveals bilayer
4 characteristics, but with distinct 2D and G band intensity ratio (I_{2D}/I_G) of ~ 2.89 and
5 0.51 , respectively. These Raman features indicate that the bilayer graphene grains at
6 sites 2 and 3 corresponds to AB Bernal stacking and non-AB twisted stacking
7 respectively¹⁸⁻¹⁹. We have also performed Raman mapping to get a full map of the
8 nucleus structure, shown in figs.3e-g. Accordingly, the 2D peak intensity map shows
9 only two main areas, corresponding to the Bernal stacking and non-AB twisted
10 turbo-stacking modes, demonstrating high uniformity in those respective areas. It
11 appears that the D band intensity is also weakly dependent on the stacking order²⁰, as
12 we can clearly observe the outline of those two regions in the D band map in fig. 3g.
13 Those results confirm that our controlled oxidation process breaks monolayer
14 graphene but has introduced only insignificant amount of defects on the bilayer
15 nucleus.

16
17 Previous reports show that monolayer graphene are stable in air at temperature up
18 to $400\text{ }^\circ\text{C}$ on silicon substrate²¹. The fact that we can “remove” the monolayers, *i.e.* to
19 break continuous monolayer into discontinued fragments that disrupt their structure
20 continuity, at only 300°C suggests that it is possible to lower oxidation resistance of
21 monolayers at appropriate conditions. The key feature in our method is that we
22 utilized the intrinsic reactivity difference between various numbers of layers, which is

1 further amplified by their curvatures induced by their supporting metal surface, which
2 is larger for monolayers than multi-layer structures²². Reactivity of carbon nanotube
3 or fullerene, compare with flat graphene structures, was shown to enhance remarkably
4 because of curvature²³⁻²⁴. Other contributing factors may include enhancement from
5 the underneath copper substrate and/or defects in CVD graphene²⁵. More recent work
6 has shown that the reactivity of graphene can be greatly enhanced by the substrate.²⁶
7 Other morphological features such as the graphene wrinkles, which enhances the
8 reactivity due to curvature effect, can also play very important roles under oxidation
9 environment²⁷. It would be difficult to completely remove all the resulted monolayer
10 fragments, however, the small sizes of those fragments, normally within hundreds of
11 nanometers, will disrupt the structure continuity and thus disrupt electrical/thermal
12 connectivity, in contrast to the only insignificantly damaged bilayers.

13 Electric transport measurement was conducted to investigate the electronic
14 properties of the bilayer graphene structures obtained with this approach. We used
15 Electron Beam Lithography (EBL) to fabricate bilayer graphene field effect transistor
16 (FET) in a hall bar geometry shown in **Figure 4a**, after the post-oxidation bilayer
17 graphene was transferred onto 300nm oxide silicon wafer. Before electrodes (10 nm
18 Ti and 40 nm Au) were deposited, the graphene sample was annealed in vacuum
19 system to improve the contact between graphene and substrate. Figure 4 illustrates the
20 sheet resistance as a function of gate voltages measured under a vacuum of 10 Torr at
21 temperature 2K, 100K, 200K and 300K. All four curves show typical ambipolar
22 behavior of graphene FET devices, confirming the high quality of bilayer graphene

1 prepared with this method. The mobility is determined to be $\mu_e = 3520$
2 ($\mu_h = 3490$) and $\mu_e = 3750$ ($\mu_h = 3590$) $\text{cm}^2 \cdot \text{v}^{-1} \cdot \text{s}^{-1}$ respectively at 300K and 2 K,
3 significantly higher than the reported RT value of $\sim 500 \text{ cm}^2 \cdot \text{v}^{-1} \cdot \text{s}^{-1}$ for LPCVD^{3,28}, and
4 recent bilayer graphene in the range of 1400-4400²⁹, compared to defect-free
5 mechanically exfoliated bilayer graphene³⁰. Here the carrier mobility was obtained by
6 the equation $\mu = (1/C_g) \partial \sigma / \partial V_g$, where $\sigma = 1/\rho_{xx}$ is the sheet conductance and
7 $C_g = 1.15 \times 10^{-8} \text{ F/cm}^2$ is the back gate capacitance. Moreover, we investigated the
8 Quantum Hall effect (QHE) on the device to study the quality of the bilayer graphene.
9 Figure 5b plots the longitudinal resistance (R_{xx}) and Hall resistance (R_{xy}) as a function
10 of the back gate voltage which was measured at 2 K with a perpendicular magnetic
11 field $B = 9 \text{ T}$. Pronounced plateaus can be clearly seen in the Hall resistance $R_{xy} =$
12 $\pm h/4Ne^2$ with $N \geq 1$, which are accompanied by the oscillations in the longitudinal
13 resistance R_{xx} . The well-shaped and symmetric QHE indicates a high quality of our
14 CVD bilayer graphene, comparable to the mechanically exfoliated bilayer graphene³¹.

15

16 Conclusions

17 In summary, here we developed a simple method to directly visualize bilayer
18 graphene nucleus on the growth Cu substrate. With this method, we were able to
19 visualize the structure of bilayer nucleus on copper by controlled oxidation in air. The
20 key is that we utilize the lower oxidation resistance for monolayer graphene, which is
21 further enhanced by the induced mechanical strain applied from the underneath
22 oxidized Cu nanoparticles. On the other hand, the structure of bilayer graphene is less

1 affected as confirmed by Raman and electronic transport measurement. The
2 visualization technique reported here gives us a tool to fast observe the nucleation
3 formation process in the chemical vapor deposition, and would enable fundamental
4 study of graphene growth with controlled number of layers by providing statistically
5 important information about graphene growth.

6

7

1 **Methods**

2 **Copper foil pretreatment** Here we use copper foil purchased from Alfa Aesar
3 (Stock no. 13382) to synthesize graphene grains. Copper foil was cut into small size
4 (around 2cm × 8 cm) and then chemically polished with FeCl₃ (5g FeCl₃, 10 mL
5 HCl and 100 mL DI water) in ultrasonic for 10-15 seconds. After that, polished
6 copper foil was rinsed with DI water for at least three times to remove residues.
7 Finally, copper foil was blow-dried with nitrogen.

8 **Graphene synthesis by chemical vapor deposition** Polished copper foil was
9 loaded into 1 inch diameter quartz tube and purge with 350 sccm high-purity argon
10 gas for at least 20 minutes. The system temperature were then ramp to 1050 °C
11 within 30 minutes, followed by charging with 15 sccm high-purity hydrogen and 15
12 sccm methane (500ppm in Ar) and kept for 1 hour to grow large sized graphene
13 grains.

14 **Graphene transfer** Graphene is transferred by electrochemical method, similar as
15 previous report³². 1 M NaOH is used as electrolyte, while saturated calomel electrode
16 and Pt are used as reference and counter electrodes, respectively.

17 **Characterizations** SEM was done using a JEOL 6390 scanning electron
18 microscope operated at 20 keV. The Raman spectrum was recorded with a Renishaw
19 Raman RM3000 scope using a 514 nm excitation argon laser. Mapping condition:
20 20×objectives lens, with 1.5 μm step in both X and Y axis. AFM was scanned under
21 semi-contact mode using a NTEGRA probe NanoLaboratory (NT-MDT, Inc.) with
22 ACTA tips from AppNano at 1.5 Hz scan rate and 512×512 resolutions. Optical

1 images were taken by a LEICA DFC 290 optical microscope.

2 **Device fabrication and electronic measurement** Graphene layers, after being
3 transferred onto the 300 nm oxide Si wafer, was first defined into the Hall Bar
4 geometry by using e-beam lithography (Raith e-LiNE, 10 kV) and then etched by
5 oxygen plasma³³. Metal contacts were defined by a second e-beam lithography step
6 followed by e-beam evaporation of 10 nm Ti and 40 nm Au. The contact resistance is
7 usually on the order of several hundred Ohms. All the measurements were carried out
8 in Physical Property Measurement System (PPMS, Quantum Design). Before
9 measurement, graphene samples were heated in situ to 380 K in high vacuum for
10 several hours to remove the adsorbed water molecules and PMMA residues. Electrical
11 measurements were carried out by using a Keithley 6221 AC/DC source and a
12 Keithley 2182A nanovoltmeter. Four-probe method was used during measurement to
13 avoid contact resistance.

14 **Acknowledgements.** This project is supported by the Research Grant Council of
15 Hong Kong SAR of Project number 623512 and DAG12EG05, Grant No.
16 SRFI11/SC02 and HKUST9/CRF/08. Technical assistance from the Materials
17 Characterization and Preparation Facilities is greatly appreciated.

18

19

20

21

22

1 Reference

- 2 1 T. Ohta, A. Bostwick, T. Seyller, K. Horn, E. Rotenberg, *Science* 2006, **313**,
3 951-954.
- 4 2 L. X. Liu, H. L. Zhou, R. Cheng, W. J. Yu, Y. Liu, Y. Chen, J. Shaw, X. Zhong, Y.
5 Huang, X. F. Duan, *ACS Nano* 2012, **6**, 8241-8249.
- 6 3 K. Yan, H. L. Peng, Y. Zhou, H. Li, Z. F. Liu, *Nano Lett.* 2011, **11**, 1106-1110.
- 7 4 H. L. Zhou, W. J. Yu, L. X. Liu, R. Cheng, Y. Chen, X. Q. Huang, Y. Liu, Y. Wang,
8 Y. Huang, X. F. Duan, *Nat. Commun.* 2013, **4**, 2096.
- 9 5 L. Gan, Z. T. Luo, *ACS Nano* 2013, **7**, 9480-9488.
- 10 6 Y. F. Hao, M. S. Bharathi, L. Wang, Y. Y. Liu, H. Chen, S. Nie, X. H. Wang, H.
11 Chou, C. Tan, B. Fallahazad, H. Ramanarayan, C. W. Magnuson, E. Tutuc, B. I.
12 Yakobson, K. F. McCarty, Y. W. Zhang, P. Kim, J. Hone, L. Colombo, R. S. Ruoff,
13 *Science* 2013, **342**, 720-723.
- 14 7 C. C. Jia, J. L. Jiang, L. Gan, X. F. Guo, *Sci Rep* 2012, **2**, 707.
- 15 8 X. S. Li, W. W. Cai, J. H. An, S. Kim, J. Nah, D. X. Yang, R. Piner, A. Velamakanni,
16 I. Jung, E. Tutuc, S. K. Banerjee, L. Colombo, R. S. Ruoff, *Science* 2009, **324**,
17 1312-1314.
- 18 9 K. S. Novoselov, A. K. Geim, S. V. Morozov, D. Jiang, Y. Zhang, S. V. Dubonos, I.
19 V. Grigorieva, A. A. Firsov, *Science* 2004, **306**, 666-669.
- 20 10 P. Blake, E. W. Hill, A. H. C. Neto, K. S. Novoselov, D. Jiang, R. Yang, T. J. Booth,
21 A. K. Geim, *Appl. Phys. Lett.* 2007, **91**, 063124.
- 22 11 X. C. Jiang, T. Herricks, Y. N. Xia, *Nano Lett.* 2002, **2**, 1333-1338.

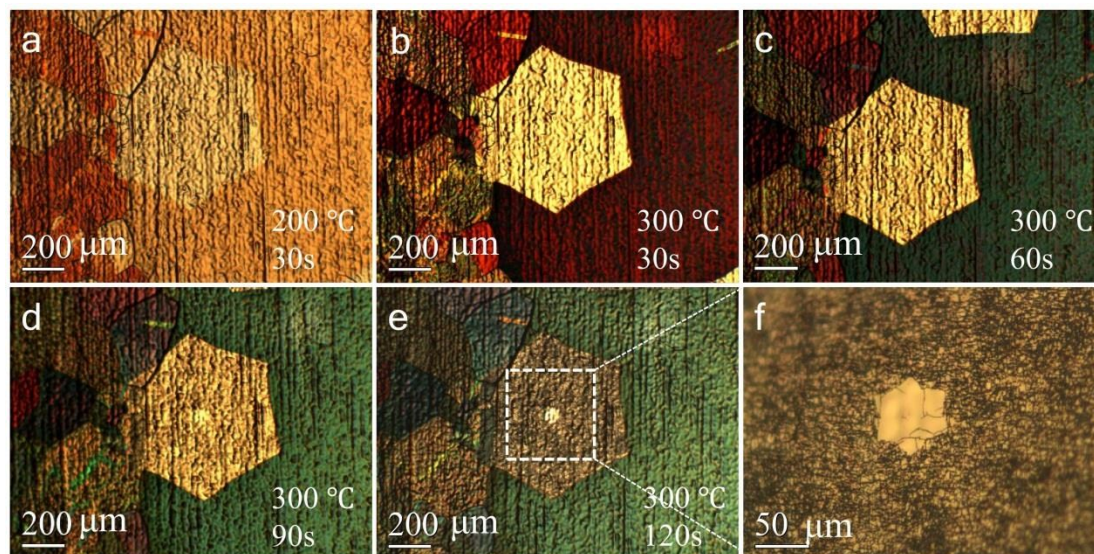
- 1 12 Y. C. Shin, J. Kong, *Carbon* 2013, **59**, 439-447.
- 2 13 J. S. Bunch, S. S. Verbridge, J. S. Alden, A. M. van der Zande, J. M. Parpia, H. G.
- 3 Craighead, P. L. McEuen, *Nano Lett.* 2008, **8**, 2458-2462.
- 4 14 P. Wu, X. F. Zhai, Z. Y. Li, J. L. Yang, *J. Phys. Chem. C* 2014, **118**, 6201-6206.
- 5 15 G. H. Han, F. Gunes, J. J. Bae, E. S. Kim, S. J. Chae, H. J. Shin, J. Y. Choi, D.
- 6 Pribat, Y. H. Lee, *Nano Lett.* 2011, **11**, 4144-4148.
- 7 16 L. Gao, J. R. Guest, N. P. Guisinger, *Nano Lett.* 2010, **10**, 3512-3516.
- 8 17 M. Schriver, W. Regan, W. J. Gannett, A. M. Zaniewski, M. F. Crommie, A. Zettl,
- 9 *ACS Nano* 2013, **7**, 5763-5768.
- 10 18 K. Kim, S. Coh, L. Z. Tan, W. Regan, J. M. Yuk, E. Chatterjee, M. F. Crommie, M.
- 11 L. Cohen, S. G. Louie, A. Zettl, *Phys. Rev. Lett.* 2012, **108**, 246103.
- 12 19 J. S. Hwang, Y. H. Lin, J. Y. Hwang, R. L. Chang, S. Chattopadhyay, C. J. Chen, P.
- 13 L. Chen, H. P. Chiang, T. R. Tsai, L. C. Chen, K. H. Chen, *Nanotechnology* 2013, **24**,
- 14 015702.
- 15 20 R. Rao, R. Podila, R. Tsuchikawa, J. Katoch, D. Tishler, A. M. Rao, M. Ishigami,
- 16 *ACS Nano* 2011, **5**, 1594-1599.
- 17 21 L. Liu, S. M. Ryu, M. R. Tomasik, E. Stolyarova, N. Jung, M. S. Hybertsen, M. L.
- 18 Steigerwald, L. E. Brus, G. W. Flynn, *Nano Lett.* 2008, **8**, 1965-1970.
- 19 22 M. Yamamoto, T. L. Einstein, M. S. Fuhrer, W. G. Cullen, *ACS Nano* 2012, **6**,
- 20 8335-8341.
- 21 23 D. Srivastava, D. W. Brenner, J. D. Schall, K. D. Ausman, M. F. Yu, R. S. Ruoff, J.
- 22 *Phys. Chem. B* 1999, **103**, 4330-4337.

- 1 24 S. Park, D. Srivastava, K. Cho, *Nano Lett.* 2003, **3**, 1273-1277.
- 2 25 I. Wlasny, P. Dabrowski, M. Rogala, P. J. Kowalczyk, I. Pasternak, W. Strupinski, J.
- 3 M. Baranowski, Z. Klusek, *Appl. Phys. Lett.* 2013, **102**, 111601.
- 4 26 Q. Wang, L. Wei, M. Sullivan, S.-W. Yang, Y. Chen, *RSC Advances* 2013, **3**, 3046.
- 5 27 Y. H. Zhang, B. Wang, H. R. Zhang, Z. Y. Chen, Y. Q. Zhang, Y. P. Sui, X. L. Li, X.
- 6 M. Xie, G. H. Yu, Z. Jin, X. Y. Liu, *Carbon* 2014, **70**, 81-86.
- 7 28 S. Lee, K. Lee, Z. H. Zhong, *Nano Lett.* 2010, **10**, 4702-4707.
- 8 29 L. Liu, H. Zhou, R. Cheng, W. J. Yu, Y. Liu, Y. Chen, J. Shaw, X. Zhong, Y. Huang,
- 9 X. Duan, *ACS Nano* 2012, **6**, 8241-8249.
- 10 30 K. Zou, J. Zhu, *Phys. Rev. B* 2010, **82**, 081407.
- 11 31 K. S. Novoselov, E. McCann, S. V. Morozov, V. I. Fal'ko, M. I. Katsnelson, U.
- 12 Zeitler, D. Jiang, F. Schedin, A. K. Geim, *Nat Phys* 2006, **2**, 177-180.
- 13 32 L. B. Gao, W. C. Ren, H. L. Xu, L. Jin, Z. X. Wang, T. Ma, L. P. Ma, Z. Y. Zhang,
- 14 Q. Fu, L. M. Peng, X. H. Bao, H. M. Cheng, *Nat. Commun.* 2012, **3**, 699.
- 15 33 H. Zhang, J. Lu, W. Shi, Z. Wang, T. Zhang, M. Sun, Y. Zheng, Q. Chen, N. Wang,
- 16 J.-J. Lin, P. Sheng, *Phys. Rev. Lett.* 2013, **110**, 066805.

17

18

19



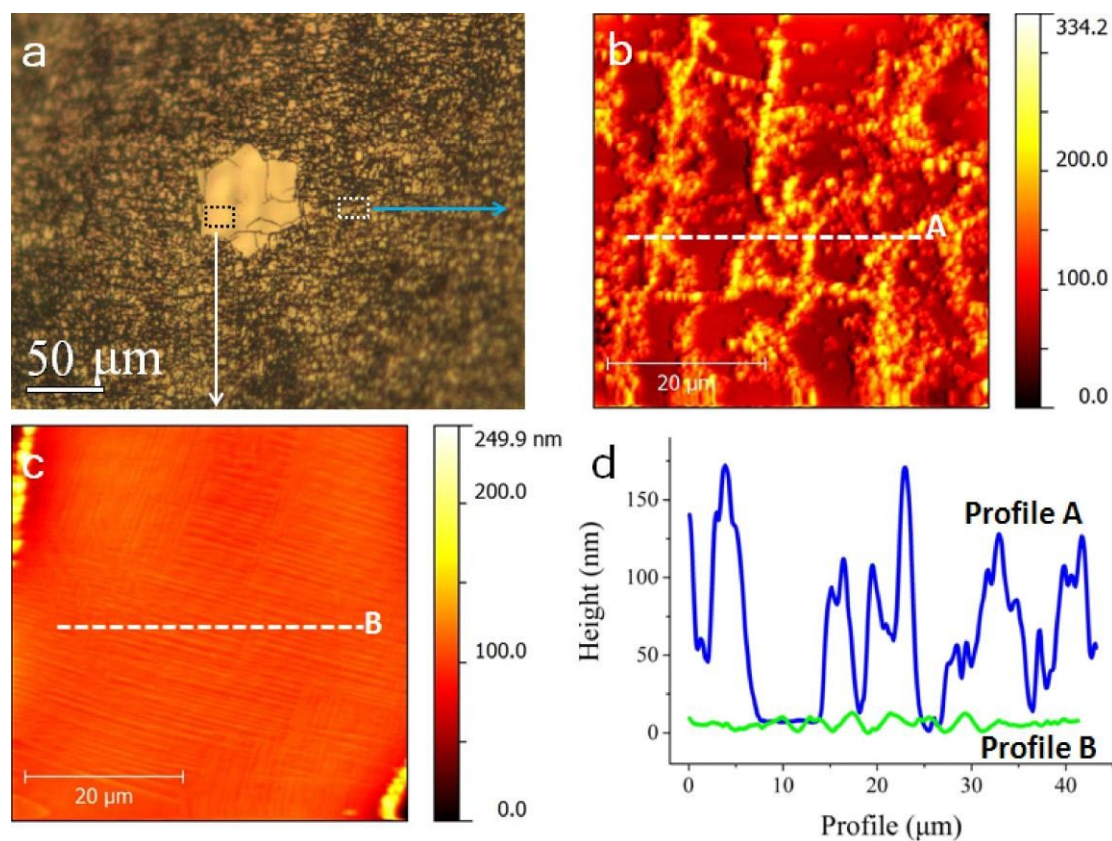
1

2 **Figure 1 | Evolution of monolayer/bilayer on copper substrate under controlled**3 **oxidation.** (a) annealing at 200°C for 30s in air. (b-e) additional annealing at 300°C in

4 air recorded at 30s, 60s, 90s and 120s. (f) Enlarged image of 3e.

5

6



1

2 **Figure 2 |Morphology comparison of monolayer and bilayer region after**3 **oxidation.** (a) Optical image for post-oxidation bilayer nucleus on copper. (b, c)

4 AFM images for grains of monolayer and bilayer nucleus regions, respectively. (d)

5 Height profiles along the lines in 2b and 2c, respectively.

6

7

8

9

10

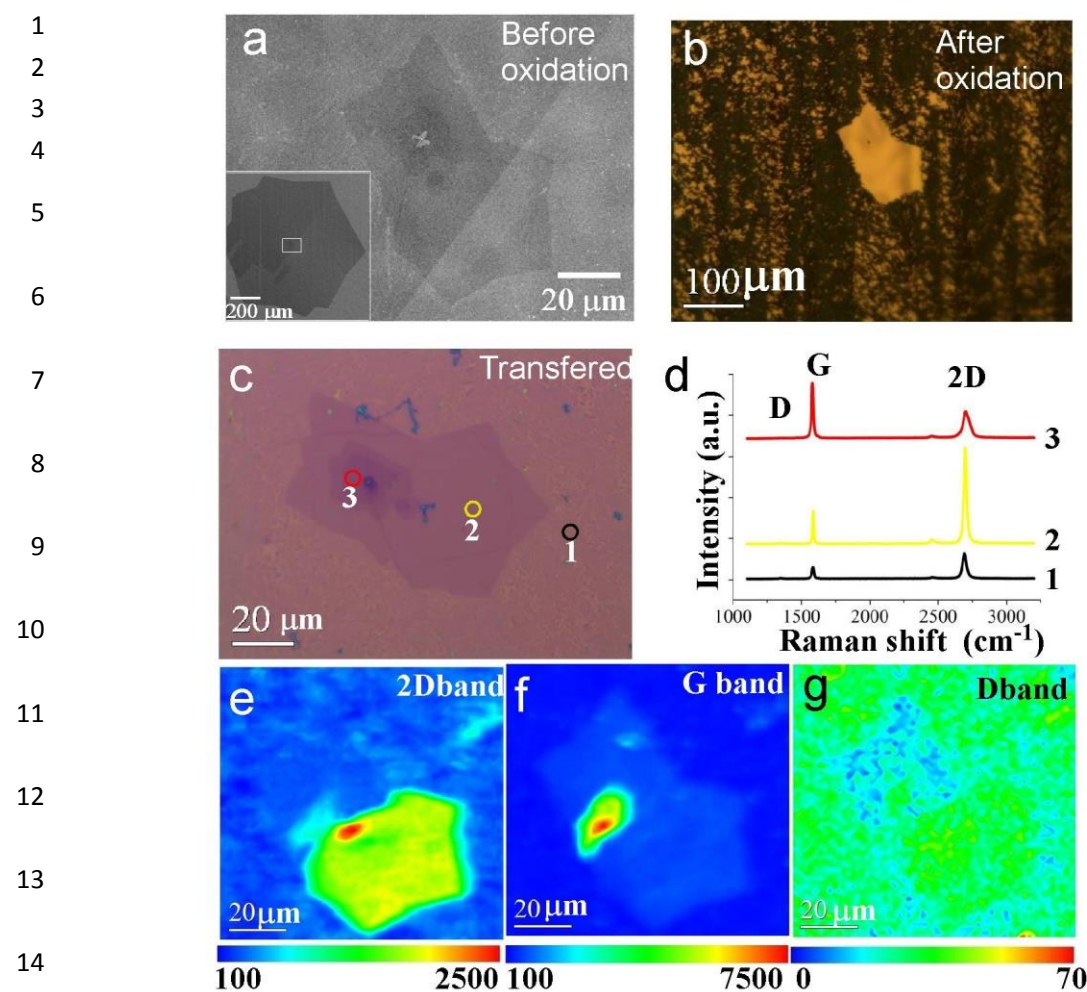
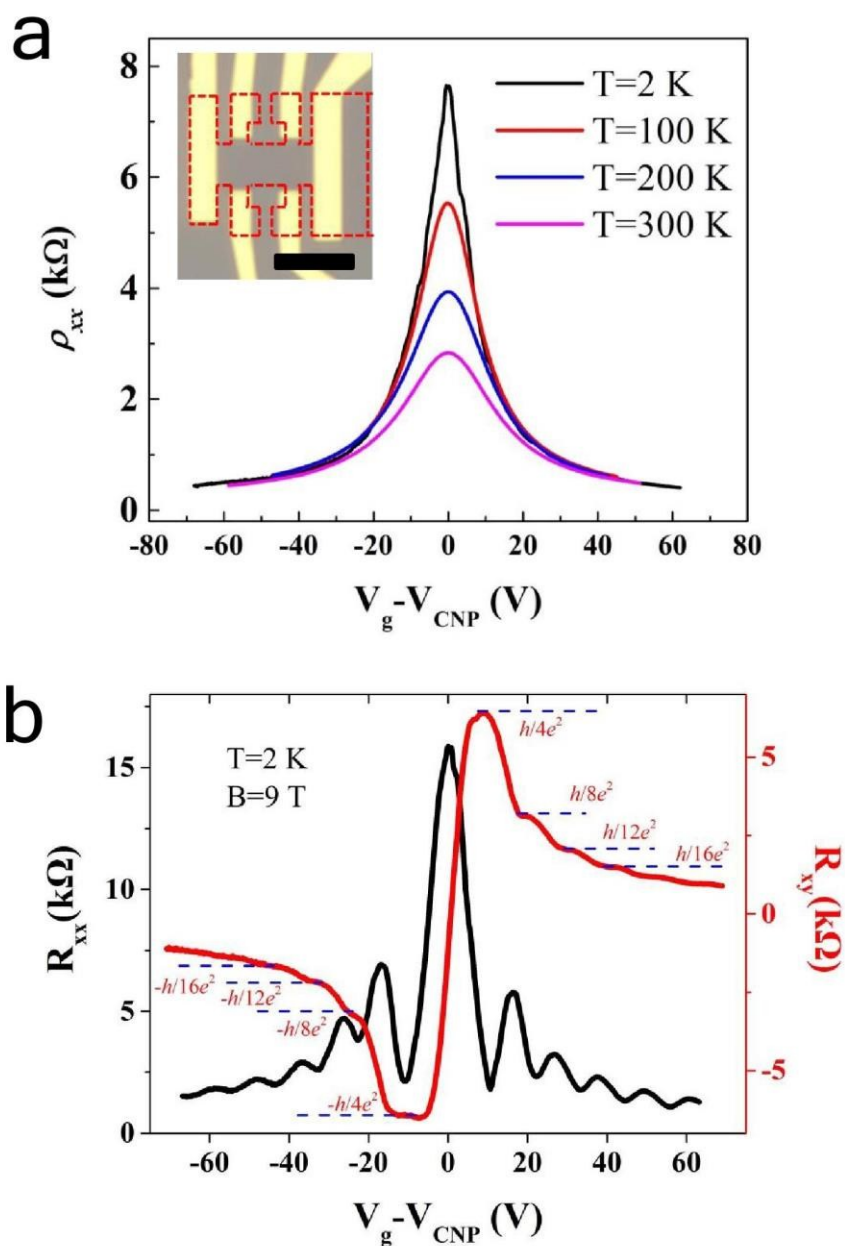


Figure 3 Bilayer/few layers properties. (a) SEM images of bilayer/few layers graphene grain on copper before oxidation. Inset indicates the overview of the whole flake. (b) Optical images for the same grain on oxidized copper (200 °C, 30s annealing in air and then additional annealing at 300 °C for 120s). (c) Optical image after transferred onto 300nm oxide substrate. (d) Raman spectrum at 3 spots on nucleus. Site 1, 2 and 3 shows monolayer fragments, typical non-AB stacking and AB stacking bilayer characteristics, respectively. (c-e) Raman mapping of 2D, G and D band for the bilayer/few layers region.

23

24



17 **Figure 4** Transport measurement of FET device of bilayer obtained by controlled
 18 **oxidation.**(a) Transport curve of nucleus-based FET device at 2, 100, 200and 300K.
 19 The inset optical image shows the configuration of device. The shape of hall bar is
 20 donated with red dot line. The scale bar in inset is 5 μ m.(b) Quantum Hall
 21 measurement at T = 2 K with a perpendicular magnetic field B = 9 T.